ChemSusChem

Research Article
doi.org/10.1002/cssc.202401758

Chemistry Europe
European Chemical Societies Publishing

www.chemsuschem.org

Boosting the O_2-to-H_2O_2 Selectivity Using Sn-Doped Carbon Electrocatalysts: Towards Highly Efficient Cathodes for Actual Water Decontamination

Lele Zhao,[a] Marco Mazzucato,[b] Sonia Lanzalaco,[c] Mattia Parnigotto,[b] Anastassiya Khan,[d] Andrea Zitolo,[d] Pere L. Cabot,[a] Christian Durante,*[b] and Ignasi Sirés*[a]

The high cost and often complex synthesis procedure of new highly selective electrocatalysts (particularly those based on noble metals) for H_2O_2 production are daunting obstacles to penetration of this technology into the wastewater treatment market. In this work, a simple direct thermal method has been employed to synthesize Sn-doped carbon electrocatalysts, which showed an electron transfer number of 2.04 and outstanding two-electron oxygen reduction reaction (ORR) selectivity of up to 98.0%. Physicochemical characterization revealed that this material contains 1.53% pyrrolic nitrogen, which is beneficial for the production of H_2O_2, and -C≡N functional group, which is advantageous for H^+ transport.

Moreover, the high volume ratio of mesopores to micropores is known to favor the quick escape of H_2O_2 from the electrode surface, thus minimizing its further oxidation. A purpose-made gas-diffusion electrode (GDE) was prepared, yielding 20.4 mM H_2O_2 under optimal electrolysis conditions. The drug diphenhydramine was selected for the first time as model organic pollutant to evaluate the performance of an electrochemical advanced oxidation process. In conventional electro-Fenton process (pH 3), complete degradation was achieved in only 15 min at 10 mA cm^{-2}, whereas at natural pH 5.9 and 33.3 mA cm^{-2}, almost overall drug removal was reached in 120 min.

Introduction

Hydrogen peroxide (H_2O_2) is an efficient green oxidizing agent, widely utilized in medicine, textile industry, industrial synthesis, and water treatment.[1,2] Within environmental protection, H_2O_2 is primarily employed in the electrochemical advanced oxidation processes (EAOPs), facilitating the in-situ generation of •OH to degrade and mineralize organic pollutants in sewage.[3,4] Against the backdrop of rapid industrial expansion and in response to global public health safety concerns, the demand for H_2O_2 has experienced a sharp escalation. By the end of 2024,

global H_2O_2 consumption is projected to reach 6 million tons,[5] with an annual growth rate of approximately 5.5%.[6] At present, 95% of industrial H_2O_2 is predominantly synthesized using the anthraquinone auto-oxidation process developed in 1939.[7] However, this approach is energy-demanding and is restricted to centralized factories. Moreover, its intricate procedure incurs costs related to dangerous H_2O_2 manipulation, storage, and transportation.[8] Considering that, for water treatment through EAOPs, H_2O_2 concentrations ranging from 3.0–15.0 mM are adequate for ensuring rapid decontamination,[9] researchers are motivated to develop simpler and more compact on-site H_2O_2 production systems.

In recent years, scholars have conducted research on direct H_2O_2 synthesis as well as on photocatalytic methods. However, drawbacks such as high risks, low light utilization, and limited transparency put constraints on their widespread implementation.[10,11] In this context, the electrochemical 2-e$^-$ oxygen reduction reaction (ORR) is explored as an appealing alternative for H_2O_2 synthesis. This approach is not only particularly well-suited for decentralized H_2O_2 production, but it has a big potential for reducing energy consumption and secondary pollution.[12] Especially in the field of the electro-Fenton (EF) process (i.e., the metal-catalyzed decomposition of H_2O_2 to yield •OH),[2] anchoring active catalytic materials onto the surface of a porous carbon cloth substrate and combining the ensemble with an air chamber to create a gas-diffusion electrode (GDE) has gained attention. In such systems, air (or pure O_2) flows from the gas chamber through the porous cloth to reach the triple-phase boundary, where the active electrocatalyst transforms it into H_2O_2, thus providing a continuous

[a] *Laboratori d'Electroquímica dels Materials i del Medi Ambient, Departament de Ciència de Materials i Química Física, Secció de Química Física, Facultat de Química, Universitat de Barcelona, Barcelona, Spain*

[b] *Department of Chemical Sciences, University of Padua, Padova, Italy*

[c] *Departament d'Enginyeria Química, EEBE Universitat Politècnica de Catalunya, Barcelona, Spain*

[d] *Synchrotron SOLEIL L'Orme des Merisiers, Saint-Aubin, France*

Correspondence: *Ignasi Sirés, Laboratori d'Electroquímica dels Materials i del Medi Ambient, Departament de Ciència de Materials i Química Física, Secció de Química Física, Facultat de Química, Universitat de Barcelona, Martí i Franquès 1–11, 08028 Barcelona, Spain.*
Email: i.sires@ub.edu

Christian Durante, Department of Chemical Sciences, University of Padua, Via Marzolo 1, 35131 Padova, Italy.
Email: christian.durante@unipd.it

Supporting information for this article is available on the WWW under https://doi.org/10.1002/cssc.202401758

ChemSusChem

Research Article
doi.org/10.1002/cssc.202401758

**Chemistry
Europe**
European Chemical
Societies Publishing

source of reactive oxygen species for efficiently applying the EF process.[13,14]

To enhance the efficiency of H_2O_2 production, researchers have focused on optimizing the 2-e$^-$ ORR, trying to disentangle the activity-selectivity trade-off.[12] Some authors have investigated various carbon-supported electrocatalytic materials, following doping strategies that allow decorating the carbon substrate with a range of metal-based structures that span from nanoparticles (NPs) to atomically-dispersed catalysts. These include metal alloys and bimetallic NPs,[15–19] metal oxides and sulphides,[20,21] metal complexes,[22] and single-atom catalysts,[23–26] which exhibit improved performance, especially among the d-block metals (fourth period),[27] as well as metal-free materials.[28,29] In all these cases, the aim is to decrease the overpotential required for ORR, as the oxygen supply is enhanced, thereby increasing the generation of H_2O_2.[26]

Stephens, Rossmeisl, and co-workers carried out a rational design of new electrocatalysts for H_2O_2 production by alloying a strong O_2-adsorbing element like Pt or Pd, with a weaker oxygen adsorbing element (Hg), thus providing optimized electronic and geometric effects.[16,17] More recently, the 2-e$^-$ ORR mechanism on Au–Pd nanoalloy surfaces has been unveiled via computational methods.[19] On the other hand, Félix-Navarro et al. deposited bimetallic Pt–Pd nanoparticles on MWCNTs; the resulting material was sprayed onto a reticulated vitreous carbon (RVC) GDE, producing 71 mM H_2O_2 in 0.5 M H_2SO_4 solution after 20 min at $E_{cath} = -0.50$ V vs Ag/AgCl.[15] Lanza's group has specialized in preparing GDEs for in-situ electrogeneration of H_2O_2 using a range of organic and inorganic carbon black modifiers. For example, they have recently reported that anchoring gold nanoparticles onto Printex L6 carbon black (PCL6), giving rise to an Au-ZrO$_2$/PL6 C hybrid support, led to a simultaneous increase in catalytic activity and selectivity (ORR onset potential of 0.34 V vs Ag/AgCl, and H_2O_2 selectivity around 97%).[30] The resulting GDE, prepared by hot-pressing of the active modified carbon between two steel sheets generated 17.6 mM H_2O_2 for 120 min in 0.1 M K_2SO_4 solution (pH 2.5) at 50 mA cm^{-2}. The Pd1%/PCL6 catalyst obtained by dispersing palladium nanoparticles on PCL6 also showed high activity, and the starting potential was 320 mV lower than that of the unmodified PCL6. Employing carbon cloth as the substrate, a certain amount of Pd1%/PCL6 was coated, followed by drying under N_2 gas flow; the accumulated H_2O_2 concentration with such GDE was 1.69-fold higher than that reached with pristine PLC6.[31] The same group, in collaboration with Santos' group, employed ruthenium and niobium oxides as carbon black modifiers to obtain 5.0% Ru$_{05}$Nb$_{95}$O/C, and the corresponding GDE yielded 8.2 mM H_2O_2 after 2 h at a current density (j) of 100 mA cm^{-2}.[32] In other works, they showed that tungsten is also an interesting surface modifier; after adding WO$_{2.72}$, the production yield increased from 67%–87%, and the energy consumption decreased.[33] Zhou's group has also made significant contributions to the manufacture of GDEs. Using carbon felt as substrate and commercial carbon black as active material, a superhydrophobic natural air-diffusion electrode (NADE) was fabricated, resulting in rapid H_2O_2 production (101.67 mg h^{-1} cm^{-2}) with high oxygen

utilization (44.5%–64.9%) and oxygen diffusion coefficients (5.7 times that of air-pumped GDEs).[34] Fe-loaded carbons have also been studied to a large extent, not only for H_2O_2 production but for simultaneous heterogeneous Fenton's reaction, as shown for carbonaceous cathodes with confined iron.[35] Apart from doping with metallic entities, heteroatoms like S and N are also known to favor the 2-e$^-$ ORR.[28,29] S and N self-doped biomass carbon (SN-BC) was obtained from discarded ginkgo biloba leaves; when applied to both sides of a carbon felt, the cumulative concentration of H_2O_2 was about 3 mM at 50 mA for 2 h.[36] In all these commented studies on GDEs, note that carbon and stainless steel are ubiquitous as substrates. However, using Ni mesh, and carbon black as the catalyst, the electroproduction of H_2O_2 after 48 h of testing showed good stability (60 mM for 25 h), whereas a gradual decline was observed with the other two supports, which must be carefully considered for GDE scale-up.[37]

Many of the metals referred above, especially the noble ones like the platinum-group metals (PGMs), are categorized as endangered elements.[38] In contrast, tin is a good example of a relatively abundant material, but no attempts to manufacture Sn-based GDEs have been reported so far.[39] An advantage of Sn, as compared to other metals with similar abundance (like Co and Ni), is its safety and environmental compatibility, since there is no evidence that tin or its compounds can cause cancer or other severe reactions in humans.[40] The price of Sn is somewhat higher than that of base metals, but in line with other widespread elements in the field of electrocatalysis like Co and Mo, making it a feasible choice. Gao et al. have recently summarized the potentialities of this metal in electrocatalytic oxidation and reduction reactions.[40] Certainly, there is a growing interest in *p*-block elements, mainly Sn, Sb, and Bi, in the field of heterogeneous electrocatalysis.[41] Regarding the ORR, the ability of Sn to form single-atom catalysts (M–N–C materials), aiming at replacing precious metals in PEMFCs, promising results have been evidenced as compared to classical Fe–N–C catalysts.[42] The effectiveness of single-atom catalysts based on Sn has been shown computationally,[43] and also as a possible co-catalyst with Fe for ORR.[44] Tin can form highly stable Sn–C bonds and exhibits strong adsorption affinity for O_2, which might bring about bright perspectives for accelerating the O_2 electroreduction, as demonstrated even under alkaline conditions.[45,46] More specifically, N-doped tin catalysts supported on commercial carbon black (XC72) have demonstrated improved half-wave potentials and higher j values under alkaline conditions,[27] which seems clearly advantageous for utilizing this type of material for H_2O_2 production for water treatment under near-neutral conditions.

Aiming to expand the operational pH window for in-situ H_2O_2 electrosynthesis using GDEs, a set of SnC catalysts has been prepared in this work. First, a comprehensive physico-chemical characterization of the synthesized catalysts was carried out, whereas their O_2-to-H_2O_2 activity and selectivity at neutral pH were assessed via rotating ring-disk electrode (RRDE) tests. The best electrocatalyst was selected to manufacture a GDE, in order to evaluate its ability to produce H_2O_2 in electrolytic assays at constant j. Moreover, diphenhydramine

(DPH), a first-generation antihistamine with good inhibitory effects on allergies and vomiting, was selected as a target contaminant to investigate the performance of the electro-Fenton (EF) process for the first time. DPH cleavage is incomplete during wastewater treatment, being detected in 25% of downstream surface water samples, with a maximum concentration of about 45 ng L^{-1}.[47,48] Municipal wastewater treatment removes only about 69% of DPH present in the influent.[49,50]

Results and Discussion

Three Sn-doped carbon electrocatalysts were synthesized following the procedure depicted in Figure S1: sample named SnC1 was obtained upon direct pyrolysis of the mixture between a prepared Sn salt and commercial Vulcan XC72 conductive carbon black, at 900°C for 2 h; SnC2 resulted from acid pickling of the previous sample; and SnC3 was obtained after repyrolysis of the latter sample at 900°C for 2 h. Vulcan XC72 was also investigated for comparison. Details of the synthesis protocol are given in the Supporting Information file.

Electrochemical Performance of the Catalysts

The ORR performance of the three SnC electrocatalysts and the commercial carbon black was investigated by linear sweep voltammetry (LSV) measurements. The H_2O_2 oxidation current was collected at the ring of an ink-modified RRDE and, consequently, the dependence of the H_2O_2 selectivity and the electron transfer number were calculated as described in Text S5 of the SI file. The ring collection efficiency (N) was determined as 24.6% from LSV curves obtained with the RRDE (Figure S2). Regarding the O_2 reduction assays, as can be deduced from the low onset potential ($E_{onset} = 331.9$ mV, Table S1 and Figure 1a), Vulcan XC72 exhibited the poorest ORR activity. The onset potential was significantly improved upon Sn doping, suggesting that the introduction of Sn is certainly beneficial to improve the ORR activity at near-neutral pH. In particular, SnC1 and SnC2 exhibited a similar E_{onset} of 0.536 and 0.525 mV, respectively. It can also be seen from Figure 1b and Table S1 that those two catalysts had similar electron transfer numbers, very close to optimum $n = 2$, thus yielding very high O_2-to-H_2O_2 selectivities close to 100%. It is also evident that SnC1 and SnC2 outperformed SnC3, in terms of both activity and selectivity. Nonetheless, it can be concluded that the three SnC electrocatalysts behaved positively, presumably showing an outstanding ability to electrogenerate H_2O_2 in an efficient manner as compared to XC72.

Physicochemical Characterization

The general XPS spectra of Vulcan XC72 and the three SnC catalysts can be observed in Figure S3. Trace Sn contents below 0.1 at.% were found in SnC1 and SnC2, in contrast to the much
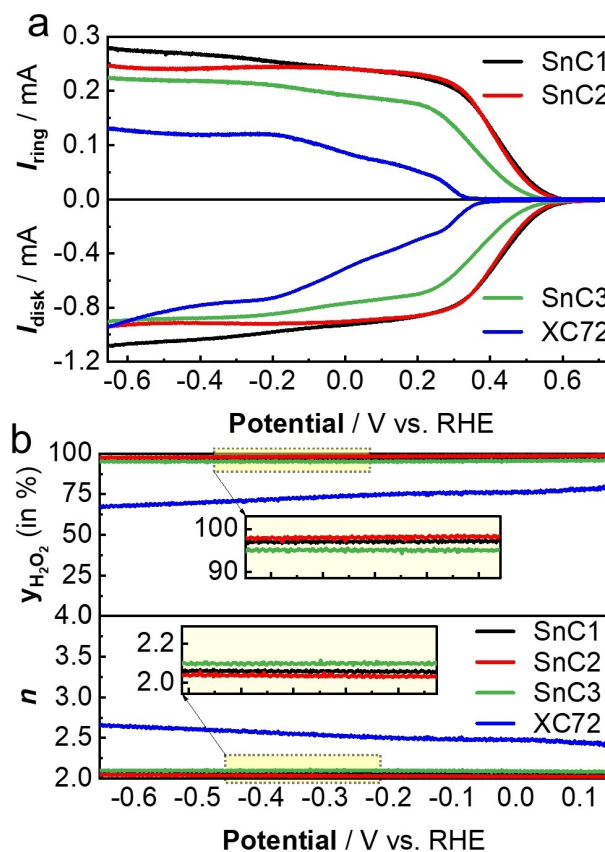

Figure 1. a) Linear sweep voltammograms obtained at an RRDE modified with either Vulcan XC72 carbon black, SnC1, SnC2, or SnC3. The electrocatalysts were drop-cast on the GC disk (catalyst loading: 0.6 mg cm^{-2}), and voltammograms were recorded in an O_2-saturated 0.1 M Na_2SO_4 electrolyte at natural pH 5.9, at $v_{scan} = 10$ mV s^{-1}. b) Top plot: H_2O_2 selectivity; bottom plot: number of transferred electrons. These two parameters were determined from the data of plot (a) at 1600 rpm, at $E_{ring} = 1.54$ V vs. RHE. A graphite rod and Ag|AgCl (3 M KCl) were used as CE and RE, respectively.

stronger peak appearing in the spectrum of SnC3 (Sn content close to 1%). The latter is partly due to better exposure of the Sn-containing sites/particles upon the second thermal treatment. A clear increase in the N content can also be observed from the spectra of the Sn-doped materials, as compared to the spectrum of Vulcan XC72, which supports the positive role of phenanthroline as an N-doping source during the synthesis. The N content was superior in SnC2, reaching almost 2 at.%. The high-resolution XPS spectra and the deconvolution results for N 1s are shown in Figure 2a–d. Pyridinic and graphitic N seemed to be present in XC72, although they could not be reliably quantified due to the uncertainty in the measurement; greater amounts of both types of N were attained in SnC1 and SnC3, which is relevant because graphitic N is one of the key factors to promote the synthesis of H_2O_2. However, a more crucial role in ORR is played by pyrrolic N.[51,52] The SnC2 catalyst presented this type of N in a relatively high amount (above 1.5 at.%), along with a small amount of oxidized N that resulted from the acid pickling applied for its synthesis. Figure S4 summarizes the distribution of the different N types. On the other hand, the deconvolution of Sn 3d peaks (i.e., Sn 3d$_{3/2}$ and
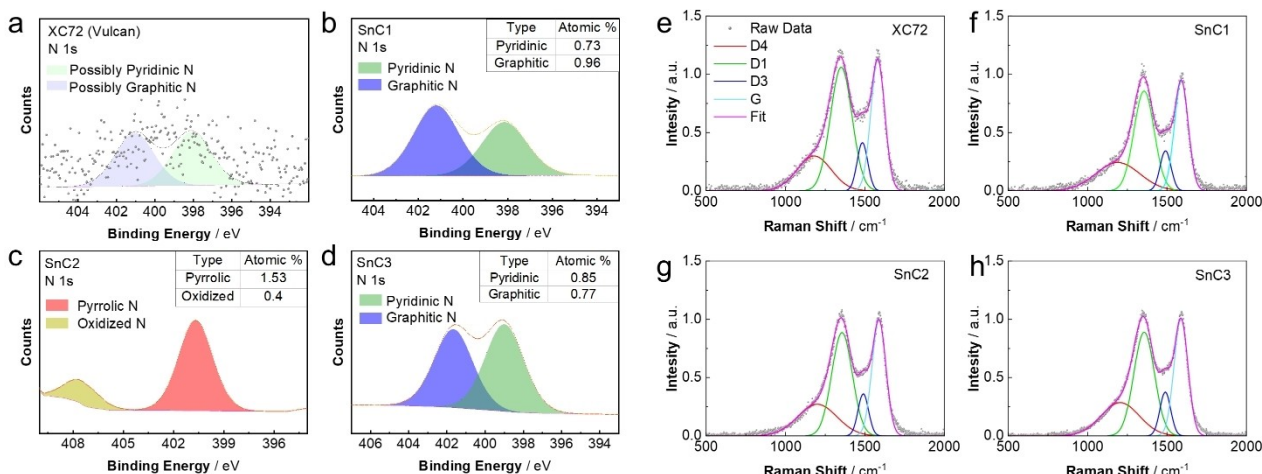
ChemSusChem

Research Article
doi.org/10.1002/cssc.202401758

Chemistry
Europe
European Chemical
Societies Publishing

Figure 2. High-resolution XPS spectra of N 1s for (a) XC72, (b) SnC1, (c) SnC2, and (d) SnC3. Deconvoluted Raman spectra of (e) XC72, (f) SnC1, (g) SnC2, and (h) SnC3.

Sn $3d_{5/2}$ at higher and lower binding energy, respectively) is shown in Figure S5, showing the presence of Sn^{4+} in all the Sn-doped carbons, alongside a very weak Sn^0 signal that could only be detected in SnC3. From this figure, it is clear that the surface of all the prepared electrocatalysts becomes easily oxidized upon contact with air; however, such an oxidation is only superficial, as demonstrated by the bulk particle analysis confirming the presence of metal in SnC1 and SnC3 (Figure 3a).

Raman characterization was then employed to gain information on the graphitization degree of the four carbonaceous materials in terms of the degree of crystallinity (i.e., predominance of sp^2 or sp^3 configuration). Carbon black is usually describable as nanocrystalline graphite, namely, particles composed of an ordered graphitic domain of tens of nanometers in dimension interrupted by surface and edge defects. In addition, a certain amount of amorphous carbon is frequently present, which can be related to polycyclic aromatic compounds regarded as graphene layer precursors. Therefore, the deconvolution of Raman spectra of metal-doped carbon-supported catalysts is useful to evaluate the effects of the metal on the graphitization degree. Note that the use of high temperatures during synthesis and possible metal-catalyzed reactions could bring about the modification of the carbon, as has been reported in the case of Fe.[53] For the materials prepared in the present work, the most common five bands were sufficient to describe the main features of the carbon surface. These bands include so-called D1, D2, and D4, which are linked with disordered graphitic lattice, D3 that accounts for amorphous carbon, and G, which is linked to ideal graphite lattice. Figure 2e–h and Table S2 summarize, respectively, the deconvoluted bands and the calculated parameters for the sole Vulcan XC72 and the three SnC catalysts. The position of the G band and the D1-to-G intensity ratio are linked with the properties of the material, as described by Ferrari,[54] indeed recognizing material spanning from graphite to defective diamond. For reference, note that carbon black materials typically show a G band around 1590 cm^{-1} and an I_{D1}/I_G ratio close to 1, which may become lower when transitioning toward
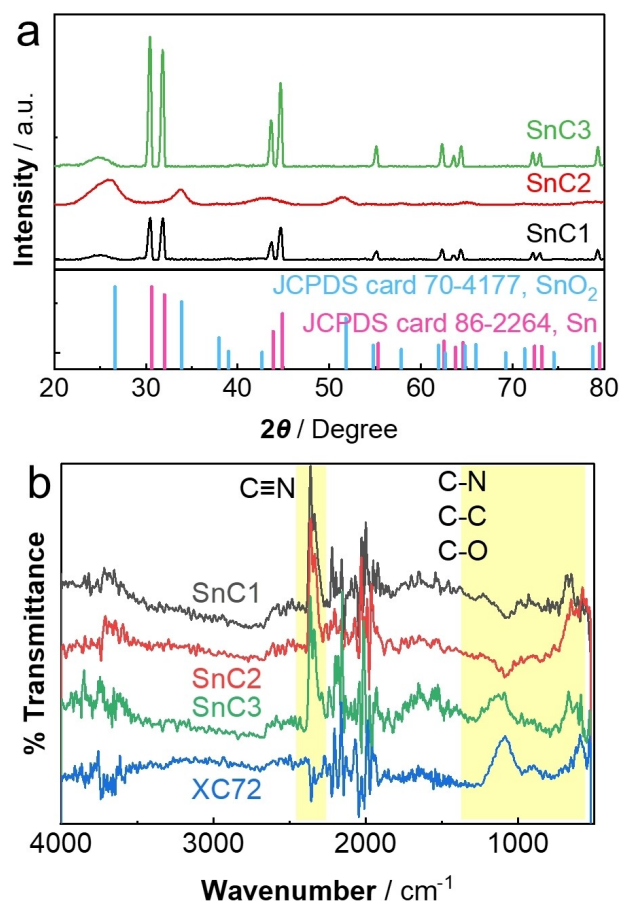

Figure 3. (a) Powder X-ray diffractograms of SnC1, SnC2, and SnC3, as compared to reference patterns of Sn and SnO_2. (b) FT-IR spectra of XC72, SnC1, SnC2, and SnC3.

pure graphite. The latter parameter can also be presented as the ratio between D1 intensity or area and that of other bands (D1, G, and D2) and is called R2;[55,56] it assumes a value higher than 0.5 for a poorly organized structure and lower than 0.5 for a well-organized one. In Table S2, considering the position of

ChemSusChem

Research Article
doi.org/10.1002/cssc.202401758

**Chemistry
Europe**
European Chemical
Societies Publishing

the D1 and G bands, their intensity ratio, and the R2 parameter, it can be concluded that no significant variations occurred upon Sn doping, apart from a slight increment of the graphitization degree. The amorphous content, evaluated as the percentage of the total spectra area, remained around 8% (Table S2), thus concluding that the amorphous carbon did not change. This permits to exclude the effect of the presence of Sn on the graphitization of the carbon, unlike that observed for other metals like iron.[53] It is also worth remarking that for SnC2, a longer acquisition time was recorded to evaluate the possible presence of SnO_2 (plausible from the acid pickling step), but a signal at around 630 cm^{-1} was not observed.

The XRD analysis evidenced a clear transition from metallic Sn to SnO_2 and then, metallic Sn again, when moving forward from SnC1–SnC2 and, finally, SnC3 (Figure 3a). In other words, SnC2 was characterized by the presence of SnO_2, with no mixed phases observed in each diffractogram. Another important difference was the particle dimensions or, better said, the crystalline domain dimensions, being around 25 nm for SnC1 and SnC3 and around 4 nm for SnC2. The formation of the metallic phase in SnC1 was induced by the presence of C as strong reductant at high temperature (pyrolysis at 900 °C in N_2), which occurred in concomitance with partial C oxidation to CO and/or CO_2 gases. The acid washing employed to synthesize SnC2 favored the oxidation of Sn to SnO_2, probably through a mechanism that involved the destruction of the bigger nanoparticles since it caused a significant reduction in nanoparticle size (i.e., one order of magnitude lower). The last step to produce SnC3 caused a further reduction of SnO_2 to metallic Sn, catalyzed by the presence of carbon that allowed the removal of the oxygen as a CO_2/CO mixture. Note that the peak at around 26° is associated with the C support, being less marked in SnC1 and SnC3 simply because of the sharper Sn peaks, for byrather than the result of a less crystalline in carbon.

The functional groups present in the synthesized catalysts were ascertained by FT-IR (Figure 3b). Worth highlighting, an adsorption band at 2362 cm^{-1} was observed in SnC1, SnC2, and SnC3, which is attributed to the stretching vibrations of C≡N, a group that is known to promote the adsorption of H^+,[57] which is expected to synergistically accelerate the H_2O_2 electrogeneration because H^+ is needed for its formation.

The specific surface area of the electrocatalysts was determined by BET analysis, and detailed information on the pore size distribution was obtained by means of the Quenched Solid Density Functional Theory (QSDFT) model, which is more accurate than the Non-Local Density Functional Theory (NLDFT).[58–60] This is because it takes into account the roughness of the surface and chemical heterogeneity, being more suitable for disordered carbons. The total pore volume was determined by applying the Gurvitsch law at $P/P_0 \approx 0.98$. The pore size distribution was determined using a slit/cylindrical pore model because it allows a better fit to the experimental data in terms of fitting error.

The shape of the isotherms (Figure 4a) offers the first indication of the properties of the four materials. For all samples, the profile can be considered as that typical of a hybrid II/III type, with H3/H4 hysteresis that is traceable to a
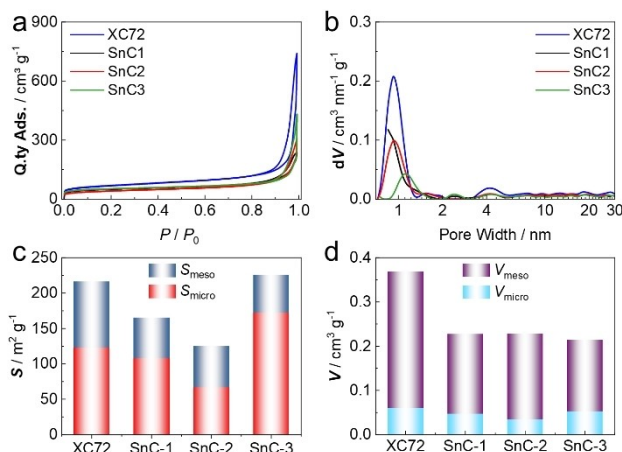

Figure 4. (a) N_2 adsorption/desorption isotherms, (b) pore size distribution, (c) specific surface area analysis along with the contribution of micropores and mesopores, and (d) pore volume analysis of micropores and mesopores for XC72, SnC1, SnC2, and SnC3.

medium-low porous material with a modest content of micro and mesopore. Moving from Vulcan XC72 to SnC3, an inverse volcano trend can be identified (note that this is clearer from the values of surface areas shown in Figure 4c); indeed, the isotherm of SnC1 is lower in adsorption with respect to XC72 within all the relative pressure range, and SnC2 is even lower, whereas for SnC3 an ascent is observed. In all samples, the presence of a small hysteresis is due to the presence of some micro and mesopores. The inclination of the isotherms in the central region of Figure 4a is instead linked to the presence of mesopores with different dimensions. With the QSDFT method, a more precise pore size distribution (PSD) has been obtained. Figure 4b shows some differences in the dimensions of the pores. To gain better information, the subdivisions in micro and mesopore surface area (Figure 4c) and volume (Figure 4d) have been extrapolated using the QSDFT method (see also Table 1). The formation of Sn nanoparticles (SnC1), their conversion into SnO_2 (SnC2), and their final reduction to Sn again (SnC3) seem to have some effect on the pore dimensions, smaller in SnC1 and bigger in SnC3. More in general, as observed from the sole isotherm, in SnC1 there is the occlusion of micro and mesopores, with the latter being more affected, probably due to the growth of the nanoparticles or other phenomena that cause the collapse of the pore network. In SnC2, mainly the micropores are affected; in this case, the SnO_2 particles may grow in proximity to micropores or smaller pores, as suggested by TEM (Figure 5, see below) and XRD (Figure 3a) analysis. In SnC3, there is a growth of micropores by widening the existing ones or by opening new ones, which can be attributed to an activation effect of SnO_2 on the carbon. The reduction of stannic oxide to metallic tin indeed entails the loss of oxygen, which is mostly released as escaping CO_2 gas with the contribution of carbon that is gradually consumed. CO_2 can further react, depending on the temperature, giving CO as the final product.[61] This is in good agreement with the fact that mesopores are very similar in amount to SnC2, since CO_2 should favor the evolution of micropores and, in addition, the regrowth

ChemSusChem

Research Article
doi.org/10.1002/cssc.202401758

Chemistry Europe
European Chemical
Societies Publishing

Table 1. Data obtained from the N_2 physisorption analysis of XC72, SnC1, SnC2, and SnC3.

	S_{BET} m^2 g^{-1}	$S_{\mu+m}$ [a] m^2 g^{-1}	S_μ [b] m^2 g^{-1}	S_m [c] m^2 g^{-1}	$V_{\mu+m}$ [a] cm^3 g^{-1}	V_μ [b] cm^3 g^{-1}	V_m [c] cm^3 g^{-1}	V_{tot} cm^3 g^{-1}
XC72	225	216	123	93	0.369	0.061	0.309	1.055
SnC1	158	166	108	58	0.228	0.047	0.180	0.356
SnC2	132	125	67	58	0.229	0.034	0.194	0.420
SnC3	170	226	172	53	0.214	0.053	0.162	0.511

[a] d < 40 nm, [b] d < 2 nm, [c] 2 nm < d < 40 nm
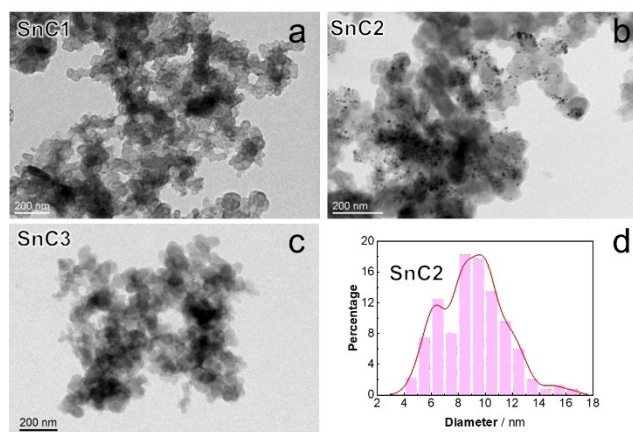
Figure 5. TEM images of (a) SnC1, (b) SnC2, (c) SnC3, and (d) particle size distribution of SnC2.

of big Sn nanoparticles (see comment on XRD above) could again bring to a mesopore occlusion. A note on SnC3 is that there is an evident discrepancy between BET and QSDFT analysis of the surface area (Table 1), which could be caused by the BET method that is not able to well describe this material. BET is a very diffuse method but, in most cases, it is not correctly applied, since it is extremely useful as a qualitative guide, but actually, it is not always quantitatively correct. For example, it should be used only for type II isotherm and having care that the C parameter is not negative,[62] which is exactly what append for SnC3, of which we report the data for completeness. This highlights the need for different methods, such as DFT ones, which can be more reliable to evaluate the surface area of some materials.

Among the four catalysts, SnC2 had the highest mesopore-to-micropore volume ratio (Figure S6). This is a very relevant feature since mesopores contribute to quickly evacuating the generated H_2O_2 as it is produced, thereby avoiding its further reduction to H_2O. Furthermore, SnC2 is the material with the most balanced mesopore-to-micropore surface ratio (Figure 4c and Table 1), which is advantageous because micropores enhance the ORR activity by offering a large number of active sites for O_2 reduction.

HRTEM and EDS were then employed to analyze the morphology and element distribution on the catalyst surface. Figure 5 depicts the representative TEM images of the SnC catalysts, which were composed of agglomerated carbon

particles. Sn particles were hardly found in SnC1 (Figure 5a) and SnC3 (Figure 5c) catalysts, whereas they could be easily detected in SnC2 (Figure 5b). Here, the Sn-based nanoparticles are irregularly distributed on the surface of the carbon particles or surrounded by carbon, forming a C-wrapped Sn-containing core structure. The size of the SnO_2 particles in the SnC2 catalyst was measured to be about 9 nm (Figure 5d).

Figure S7 shows the HRTEM images of the SnC2 catalyst, with crystal plane spacings of 0.338 nm, 0.263 nm, and 0.235 nm, corresponding to the (110), (101), and (200) crystal planes of SnO_2 (JCPDS card 70–4177), respectively. The presence of a large number of grain boundaries between these SnO_2 particles, formed by the accumulation of individual SnO_2 nanocrystals, is expected to: (i) Increase the interfacial contact between the supported electrocatalyst and the electrolyte during the electrolyzes; (ii) decrease the diffusion energy barrier toward the active sites; and (iii) facilitate the electron transfer for ORR.

The elemental distribution was confirmed by selecting a more uniform location of Sn (Figure S8): Sn and O were perfectly aligned with the particle location, being consistent with the XRD pattern. C and N were uniformly distributed throughout the region, confirming the N doping ascertained by XPS analysis.

To identify the local structure of Sn sites, ex-situ XAS measurements have been performed at the Sn K-edge for SnC1 and SnC3. Figure 6 shows the comparison of Sn K-edge XANES spectra of the investigated materials with the reference Sn foil and SnO_2 spectra. The threshold position of the spectra of SnC1 and SnC3 lies between those of Sn foil and SnO_2 (Figure 6a), indicating an intermediate oxidation state between that of the zero-valent metal and Sn^{4+}. Note that, since the curves for SnC1 and SnC3 are quite superimposable, it is expected that the tin sites are essentially formed during the first thermal treatment. Hence, the XANES spectrum of SnC2 would show no remarkable differences. Fourier Transform (FT) of the corresponding EXAFS spectra (Figure 6b) reveals a first-shell peak at 1.5–1.6 Å (uncorrected for phase shift) associated with the coordination to light atoms (O/N), whereas the presence of peaks at 2.25, 2.75 and 3.4 Å is assigned to the Sn–Sn backscattering in metallic Sn, and the peak at 3.4 Å to Sn–Sn backscattering in SnO_2, thus suggesting the coexistence of crystalline Sn and SnO_2 nanoparticles in these samples. Possibly this is due to the surface oxidation of metallic tin, as seen from XPS analysis since
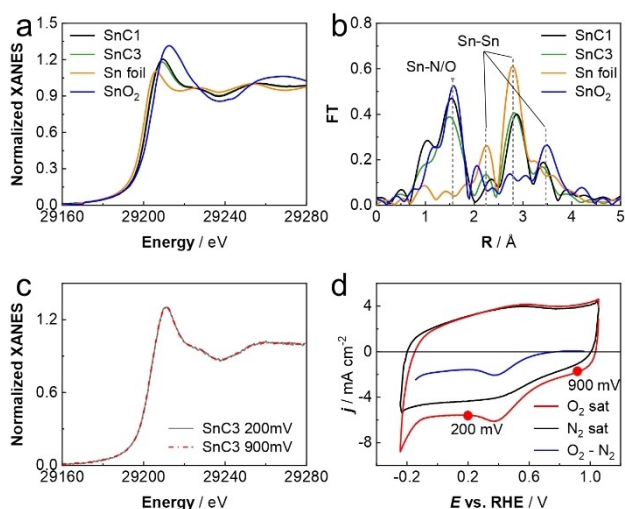
ChemSusChem

Research Article
doi.org/10.1002/cssc.202401758

Chemistry Europe
European Chemical
Societies Publishing

Figure 6. (a) Comparison between the Sn K-edge XANES experimental spectra of SnC1, and SnC3, with the reference SnO_2 and Sn foil spectra; (b) Fourier transform of the experimental EXAFS spectra of SnC1, and SnC3, with the reference SnO_2 and Sn foil spectra. (c) In situ Sn K-edge XANES spectra of SnC3 at 200 (grey curve) and 900 mV (dotted red curve) vs. RHE (O_2 saturated 0.5 M H_2SO_4 solution). (d) CVs recorded at 20 mV s^{-1} in N_2- and O_2-saturated 0.5 M H_2SO_4 solution and the difference between the two (blue line).

the metallic component was only slightly visible (Figure S5c), while XRD suggests that it is the main crystalline component.

In-situ XAS spectra of SnC3, taken as an example due to its higher tin content, have been collected at the different applied potentials in 0.5 M H_2SO_4 solution. Figure 6c demonstrates that no changes were detected in-between Sn K-edge XANES spectra at 200 and 900 mV vs. RHE. The two potentials were chosen according to CVs recorded in the in-situ cell (Figure 6d): in a zone with no oxygen reduction (900 mV vs. RHE), and a zone after the O_2 reduction peak (200 mV). This is in line with what has been previously reported for similar types of materials containing Sn-N$_x$ sites, showing independence from the applied potential.[63] Somehow, this behavior offers a first clue about the acceptable stability of the synthesized Sn-based electrocatalysts.

Preliminary H_2O_2 Production Tests

After demonstrating the appealing characteristics of the SnC materials to be employed as electrocatalysts for two-electron ORR, a first set of electrolytic trials was carried out. Aiming to evaluate the actual H_2O_2 electrogeneration performance, a closed 3-electrode cell with O_2-saturated (and continuously fed) 0.1 M Na_2SO_4 electrolyte at natural pH 5.9 was utilized (Text S6). A rotating-disk electrode (RDE) modified with each of the inks was the working electrode, thereby conducting a 10 h H_2O_2 accumulation assay at a constant potential of $E_{disk} = -0.25$ V vs. RHE ($n \sim 2$, Figure 1). To minimize immediate reduction of the generated H_2O_2 on the electrode surface, the working electrode was kept rotating at 1600 rpm throughout the process. As can be seen from Figure S9, the cumulative H_2O_2 concentration at

10 h increased in the order: SnC3 (0.12 mM) < SnC1 (0.13 mM) < Vulcan (0.15 mM) < SnC2 (0.19 mM). This result emphasizes the great relevance of combining different types of properties, as occurred with SnC2; its great ORR activity and selectivity, as well as the surface and compositional features, made it the best among all tested materials. This idea is even better exemplified by the behavior of Vulcan carbon: it was the worst in terms of electrocatalytic properties (Figure 1 and Table S1), but Figure S9 reveals that it was the second best in terms of performance under practical electrolytic operation. This can thus be explained by its non-electrochemical characteristics, especially its high V_{meso}/V_{micro} ratio (Figure S6). In the very short time framework typical of the electrochemical analysis of Figure 1, the purely electrolytic parameters determine the ranking. In contrast, once performing a long (10 h) electrolysis like that of Figure S9, the H_2O_2 accumulation is determined not only by its production (i.e., activity and selectivity of each material to electrogenerate it), but also by its ability to escape from the cathode surface and minimize its further reduction. The abundant mesopores of Vulcan contribute to preserve the H_2O_2 once produced.

GDE Manufacture and Performance

To gain deeper insight into the previous results and consider the further scale-up of the water treatment process, SnC2 was selected as the optimum electrocatalyst and then integrated into an actual GDE for bulk electrolysis testing in an undivided two-electrode cell (see experimental details in Text S7 and S8). A variety of SnC2-based 3 cm^2 GDEs was prepared using the hot pressing method (the fabrication process is schematized in Figure S10) for evaluating the effect of binder, catalyst loading, applied j, and pH on the H_2O_2 electrogeneration. The assays were made for 300 min under galvanostatic conditions.

Figure 7 shows the time course of accumulated H_2O_2 concentration using the prepared GDE in 150 mL of 0.050 M Na_2SO_4 electrolyte, in the absence of contaminants, under different conditions.

At natural pH 5.9 and $j = 33.3$ mA cm^{-2}, using a GDE with a catalyst loading of 0.5 mg cm^{-2}, the final concentration when either PTFE or Nafion was used as binder attained 20.4 and 12.2 mM H_2O_2, respectively. PTFE has obvious advantages to perform long-term electrolyzes at relatively high currents since its hydrophobicity can minimize the flooding and increase the effective contact between O_2 and electrocatalyst; in contrast, Nafion has hydrophilic channels filled with sulfonate, which is more conducive to the transport of hydrated protons. Consequently, PTFE was the binder chosen for the subsequent trials. When increasing the electrocatalyst loading (2.5 mg cm^{-2}) in the GDE, the H_2O_2 accumulation was very negatively affected, only reaching 9.3 mM at 300 min. This can be explained by the promotion of H_2O_2 electroreduction in the presence of an excess of electrocatalyst, as well as the partial blockage of the pores of the gas-diffusion layer, ending in an adverse effect. When, however, the loading was kept at 0.5 mg cm^{-2} but the applied current was reduced significantly ($j = 10$ mA cm^{-2}), the

ChemSusChem

Research Article
doi.org/10.1002/cssc.202401758

Chemistry Europe
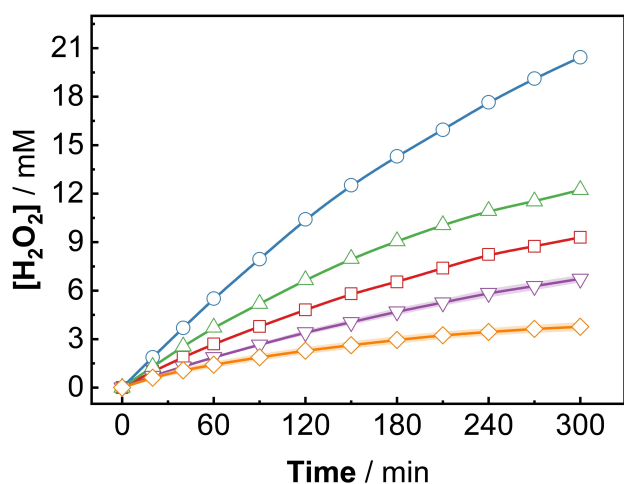European Chemical
Societies Publishing

Figure 7. H_2O_2 concentration accumulated in an undivided 2-electrode cell over the electrolysis time. The cathode was a 3 cm^2 GDE fabricated with SnC2 electrocatalyst, fed with compressed air at 0.4 L min^{-1}, and coupled to a 3 cm^2 DSA-Cl$_2$ plate as the anode. Conditions: 150 mL of a 0.050 M Na$_2$SO$_4$ solution at 25 °C. (○) Catalyst loading of 0.5 mg cm^{-2}, PTFE as the binder, $j = 33.3$ mA cm^{-2}, natural pH 5.9; (△) catalyst loading of 0.5 mg cm^{-2}, Nafion as the binder, $j = 33.3$ mA cm^{-2}, natural pH 5.9; (□) catalyst loading of 2.5 mg cm^{-2}, PTFE as the binder, $j = 33.3$ mA cm^{-2}, natural pH 5.9; (▽) catalyst loading of 0.5 mg cm^{-2}, PTFE as the binder, $j = 10$ mA cm^{-2}, natural pH 5.9; (◇) catalyst loading of 0.5 mg cm^{-2}, PTFE as the binder, $j = 10$ mA cm^{-2}, pH 3.

cumulative H_2O_2 concentration was reduced to 6.7 and 3.8 mM at natural pH 5.9 and pH 3, respectively. Nonetheless, it must be noted that those values are still sufficient to degrade the organic pollutants in Fenton-based processes,[9] which can be of interest for industrial application because the use of a lower j entails a lower energy consumption and hence, a lower operation cost.

The corresponding time course of current efficiency, calculated from the applied charge as described in previous work,[28] is shown in Figure S11. Notably, during almost the whole electrolysis period, the efficiency was higher when the GDE was manufactured under the optimum conditions (catalyst loading of 0.5 mg cm^{-2}, PTFE as the binder), especially at the lowest j. At higher j values, undesired reactions such as the 4-e$^-$ ORR and hydrogen evolution may dominate, particularly under acidic conditions, which diminishes catalytic activity. Note also that, in all trials, the current efficiency decayed over time, which is simply due to the partial H_2O_2 oxidation at the anode because of the use of an undivided electrolytic cell.

As explained above, another objective of this work was to demonstrate the effective degradation of organic pollutants by the EF process using a GDE based on these low-cost SnC electrocatalysts. Therefore, the activation of H_2O_2 was investigated under conventional EF conditions (pH 3, in the presence of 0.5 mM Fe^{2+}) and EF-like conditions (pH 5.9, in the presence of 0.1 g L^{-1} of heterogeneous Cu/C catalyst). The GDE was prepared with a catalyst loading of 0.5 mg cm^{-2} and PTFE as the binder. As shown in Figure S12, the concentrations of H_2O_2 after 300 min at $j = 10$ mA cm^{-2} were around 2 mM. This value is clearly lower than those attained in the absence of a Fenton catalyst (Figure 7), confirming the effective decomposition of

H_2O_2. In Figure S12, it can be noted that, since Cu/C is a heterogeneous catalyst, it takes a longer time to activate the H_2O_2; the concentration of H_2O_2 in the bulk rose rapidly, and from 60 min it remained almost constant.

The viability of electro-oxidation (EO), EF, and EF-like processes to degrade 14.3 mg L^{-1} (i.e., 10 mg C L^{-1}) DPH in solutions containing 0.050 M Na$_2$SO$_4$ under different electrolysis conditions is compared in Figure 8. SnC2-based GDE and DSA-Cl$_2$ served as cathode and anode, respectively. The EO process at $j = 10$ mA cm^{-2} was too weak to remove DPH, regardless of the solution pH, only yielding less than 20% concentration decay at 120 min. Operating at pH 5.9 and $j = 10$ mA cm^{-2}, the EF-like process with Cu/C as a heterogeneous catalyst was still insufficient to provide total removal of DPH, although the 75% degradation corroborates that the low H_2O_2 accumulation of Figure S11 was due to H_2O_2 activation into reactive oxygen species like •OH. Worth remarking, an increase of j up to 33.3 mA cm^{-2} allowed the greater accumulation of H_2O_2, leading to an enhanced activation as demonstrated by the almost complete DPH disappearance at 120 min. The SnC2-based GDE could also serve to treat DPH solutions under acidic conditions, as demonstrated by the fast degradation achieved by the conventional EF process at initial pH 3 and 10 mA cm^{-2}, only requiring 15 min.

Conclusions

This work demonstrates the successful preparation of low-cost and highly selective Sn-based carbons as electrocatalysts for O$_2$-to-H_2O_2 conversion. Among the synthesized materials, the one obtained from pyrolysis in the presence of an N dopant, followed by acid pickling, outperformed the others as well as
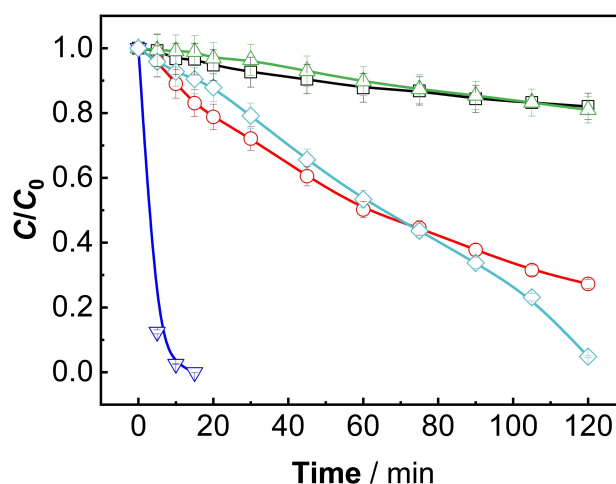

Figure 8. Time course of normalized DPH concentration during the treatment of 150 mL of solutions with 10 mg C L^{-1} drug + 0.050 M Na$_2$SO$_4$, at 25 °C, using an undivided cell with the SnC2-GDE fed with air at 0.4 mL min^{-1} and a DSA-Cl$_2$ plate as the anode. (□), Electro-oxidation process, at natural pH 5.9, $j = 10$ mA cm^{-2}. (○), EF-like process, at natural pH 5.9, with 0.1 g L^{-1} of Cu/C, $j = 10$ mA cm^{-2}. (△), Electro-oxidation, at pH 3, $j = 10$ mA cm^{-2}. (▽), EF process, at pH 3 with 0.5 mM of Fe^{2+}, $j = 10$ mA cm^{-2}. (◇), EF-like process, at natural pH 5.9, with 0.1 g L^{-1} of Cu/C, $j = 33.3$ mA cm^{-2}.

ChemSusChem

Research Article
doi.org/10.1002/cssc.202401758

Chemistry
Europe
European Chemical
Societies Publishing

commercial carbon black, exhibiting superior two-electron ORR performance. This SnC showed a better balance of N-functionalities and mesopore-to-micropore surface and volume ratio. A GDE loaded with a low amount of this electrocatalyst and PTFE as binder resulted in higher H_2O_2 accumulation, which was sufficient for the treatment of organic contaminants by the EF process, even under the most unfavorable conditions. At circumneutral pH, the EF-like process ensured the complete degradation of the drug DPH in 120 min. The excellent performance of the Sn-based GDE is promising for future scale-up of advanced electrochemical treatment of wastewater at relatively low input current.

Acknowledgements

Conflict of Interests

The authors declare no conflict of interest.

Data Availability Statement

The data that support the findings of this study are available from the corresponding author upon reasonable request.

Keywords: Electro-Fenton process · Gas-diffusion electrode · Hydrogen peroxide · SnC nanoparticles · Water treatment

[1] M. Mazzucato, C. Durante, *Curr. Opin. Electrochem.* **2022**, *35*, 101051.
[2] M. Mazzucato, A. Facchin, M. Parnigotto, C. Durante, *ACS Catal.* **2024**, *14*, 6369–6403.
[3] I. Sirés, E. Brillas, *Curr. Opin. Electrochem.* **2021**, *27*, 100686.
[4] Y. Xu, P. Xia, C. Wang, J. Cai, H. Li, Z. Ye, H. Zhang, *Chem. Eng. J.* **2023**, *462*, 142021.
[5] G.-F. Han, F. Li, W. Zou, M. Karamad, J.-P. Jeon, S.-W. Kim, S.-J. Kim, Y. Bu, Z. Fu, Y. Lu, S. Siahrostami, J.-B. Baek, *Nat. Commun.* **2020**, *11*, 2209.
[6] L. Li, L. Xu, A. W. M. Chan, Z. Hu, Y. Wang, J. C. Yu, *Chem. Mater.* **2022**, *34*, 63–71.
[7] C. Xia, J. Y. (T.) Kim, H. Wang, *Nat. Catal.* **2020**, *3*, 605–607.
[8] Y. Wen, T. Zhang, J. Wang, Z. Pan, T. Wang, H. Yamashita, X. Qian, Y. Zhao, *Ang. Chem. Int. Ed.* **2022**, *61*, e202205972.
[9] O. M. Cornejo, I. Sirés, J. L. Nava, *Electrochim. Acta* **2022**, *404*, 139621.
[10] A. P. Reyes-Cruzaley, R. M. Félix-Navarro, B. Trujillo-Navarrete, C. Silva-Carrillo, J. R. Zapata-Fernández, J. M. Romo-Herrera, O. E. Contreras, E. A. Reynoso-Soto, *Electrochim. Acta* **2019**, *296*, 575–581.
[11] X. Ren, X. Dong, L. Liu, J. Hao, H. Zhu, A. Liu, G. Wu, *SusMat* **2023**, *3*, 442–470.
[12] C. A. Martínez-Huitle, M. A. Rodrigo, I. Sirés, O. Scialdone, *Appl. Catal. B: Environ.* **2023**, *328*, 122430.
[13] O. M. Cornejo, I. Sirés, J. L. Nava, *J. Electroanal. Chem.* **2020**, *873*, 114419.
[14] Ş. Camcıoğlu, B. Özyurt, N. Oturan, D. Portehault, C. Trellu, M. A. Oturan, *Chemosphere* **2023**, *341*, 140129.
[15] R. M. Félix-Navarro, M. Beltrán-Gastélum, M. I. Salazar-Gastélum, C. Silva-Carrillo, E. A. Reynoso-Soto, S. Pérez-Sicairos, S. W. Lin, F. Paraguay-Delgado, G. Alonso-Núñez, *J. Nanopart. Res.* **2013**, *15*, 1802.
[16] S. Siahrostami, A. Verdaguer-Casadevall, M. Karamad, D. Deiana, P. Malacrida, B. Wickman, M. Escudero-Escribano, E. A. Paoli, R. Frydendal, T. W. Hansen, I. Chorkendorff, I. E. L. Stephens, J. Rossmeisl, *Nat. Mater.* **2013**, *12*, 1137–1143.
[17] A. Verdaguer-Casadevall, D. Deiana, M. Karamad, S. Siahrostami, P. Malacrida, T. W. Hansen, J. Rossmeisl, I. Chorkendorff, I. E. L. Stephens, *Nano Lett.* **2014**, *14*, 1603–1608.
[18] E. Pizzutilo, O. Kasian, C. H. Choi, S. Cherevko, G. J. Hutchings, K. J. J. Mayrhofer, S. J. Freakley, *Chem. Phys. Lett.* **2017**, *683*, 436–442.
[19] W. Liu, L. Tian, L. Shi, *J. Phys. Chem. C* **2024**, *128*, 6682–6688.
[20] S. G. F. Eggermont, R. Prato, X. Dominguez-Benetton, J. Fransaer, *React. Chem. Eng.* **2021**, *6*, 1031–1041.
[21] P. J. M. Cordeiro Junior, A. S. Martins, G. B. S. Pereira, F. V. Rocha, M. A. R. Rodrigo, M. R. V. Lanza, *Electrochim. Acta* **2022**, *430*, 141067.
[22] F. L. Silva, R. M. Reis, W. R. P. Barros, R. S. Rocha, M. R. V. Lanza, *J. Electroanal. Chem.* **2014**, *722–723*, 32–37.
[23] J. Liu, Z. Wei, Z. Gong, M. Yan, Y. Hu, S. Zhao, G. Ye, H. Fei, *Appl. Catal. B: Environ.* **2023**, *324*, 122267.
[24] Y. Wu, Y. Ding, X. Han, B. Li, Y. Wang, S. Dong, Q. Li, S. Dou, J. Sun, J. Sun, *Appl. Catal. B: Environ.* **2022**, *315*, 121578.
[25] Y.-X. Du, Q. Yang, W.-T. Lu, Q.-Y. Guan, F.-F. Cao, G. Zhang, *Adv. Funct. Mater.* **2023**, *33*, 2300895.
[26] J. Xi, S. Yang, L. Silvioli, S. Cao, P. Liu, Q. Chen, Y. Zhao, H. Sun, J. N. Hansen, J.-P. B. Haraldsted, J. Kibsgaard, J. Rossmeisl, S. Bals, S. Wang, I. Chorkendorff, *J. Catal.* **2021**, *393*, 313–323.
[27] M. Mazzucato, L. Gavioli, V. Balzano, E. Berretti, G. A. Rizzi, D. Badocco, P. Pastore, A. Zitolo, C. Durante, *ACS Appl. Mater. Interfaces* **2022**, *14*, 54635–54648.
[28] G. Daniel, Y. Zhang, S. Lanzalaco, F. Brombin, T. Kosmala, G. Granozzi, A. Wang, E. Brillas, I. Sirés, C. Durante, *ACS Sustain. Chem. Eng.* **2020**, *8*, 14425–14440.
[29] Y. Zhang, G. Daniel, S. Lanzalaco, A. A. Isse, A. Facchin, A. Wang, E. Brillas, C. Durante, I. Sirés, *J. Hazard. Mater.* **2022**, *423*, 127005.
[30] M. S. Kronka, G. V. Fortunato, L. Mira, A. J. dos Santos, M. R. V. Lanza, *Chem. Eng. J.* **2023**, *452*, 139598.
[31] G. V. Fortunato, M. S. Kronka, A. J. dos Santos, M. Ledendecker, M. R. V. Lanza, *Chemosphere* **2020**, *259*, 127523.
[32] R. B. Valim, L. C. Trevelin, D. C. Sperandio, J. F. Carneiro, M. C. Santos, L. A. Rodrigues, R. S. Rocha, M. R. V. Lanza, *J. Environ. Chem. Eng.* **2021**, *9*, 106787.
[33] E. C. Paz, L. R. Aveiro, V. S. Pinheiro, F. M. Souza, V. B. Lima, F. L. Silva, P. Hammer, M. R. V. Lanza, M. C. Santos, *Appl. Catal. B: Environ.* **2018**, *232*, 436–445.
[34] Q. Zhang, M. Zhou, G. Ren, Y. Li, Y. Li, X. Du, *Nat. Commun.* **2020**, *11*, 1731.
[35] P. Su, M. Zhou, G. Ren, X. Lu, X. Du, G. Song, *J. Mater. Chem. A* **2019**, *7*, 24408–24419.
[36] X. Wang, Q. Zhang, J. Jing, G. Song, M. Zhou, *Chem. Eng. J.* **2023**, *466*, 143283.
[37] G. Ren, S. Lanzalaco, M. Zhou, P. L. Cabot, E. Brillas, I. Sirés, *Chem. Eng. J.* **2023**, *454*, 140515.
[38] ACS, "The Periodic Table of Endangered Elements", https://www.acs.org/greenchemistry/research-innovation/endangered-elements.html. Last access: 9 October 2024.
[39] A. A. Yaroshevsky, *Geochem. Int.* **2006**, *44*, 48–55.
[40] M. Gao, X. Zhang, S. Dai, K.-W. Wang, *Inorg. Chem. Front.* **2024**, *11*, 1019–1047.
[41] C. Lv, J. Liu, J. Lee, Q. Zhu, J. Xu, H. Pan, C. Xue, Q. Yan, *ACS Nano* **2022**, *16*, 15512–15527.

[42] F. Luo, A. Roy, L. Silvioli, D. A. Cullen, A. Zitolo, M. T. Sougrati, I. C. Oguz, T. Mineva, D. Teschner, S. Wagner, J. Wen, F. Dionigi, U. I. Kramm, J. Rossmeisl, F. Jaouen, P. Strasser, *Nat. Mater.* **2020**, *19*, 1215–1223.

[43] Y. Zhang, B. Li, Y. Su, *Molecules* **2023**, *28*, 5571.

[44] F. Luo, A. Roy, M. T. Sougrati, A. Khan, D. A. Cullen, X. Wang, M. Primbs, A. Zitolo, F. Jaouen, P. Strasser, *J. Am. Chem. Soc.* **2023**, *145*, 14737–14747.

[45] X. Zhang, J. Liu, Y. Qiao, A. Kong, R. Li, Y. Shan, *Electrochim. Acta* **2019**, *320*, 134593.

[46] E. Negro, A. Bach Delpeuch, K. Vezzù, G. Nawn, F. Bertasi, A. Ansaldo, V. Pellegrini, B. Dembinska, S. Zoladek, K. Miecznikowski, I. A. Rutkowska, M. Skunik-Nuckowska, P. J. Kulesza, F. Bonaccorso, V. Di Noto, *Chem. Mater.* **2018**, *30*, 2651–2659.

[47] E. Topp, M. W. Sumarah, L. Sabourin, *Sci. Total Environ.* **2012**, *439*, 136–140.

[48] P. E. Stackelberg, E. T. Furlong, M. T. Meyer, S. D. Zaugg, A. K. Henderson, D. B. Reissman, *Sci. Total Environ.* **2004**, *329*, 99–113.

[49] S. Wolfson, A. W. Porter, T. S. Villani, J. E. Simon, L. Y. Young, *Chemosphere* **2018**, *202*, 460–466.

[50] B. Du, A. E. Price, W. C. Scott, L. A. Kristofco, A. J. Ramirez, C. K. Chambliss, J. C. Yelderman, B. W. Brooks, *Sci. Total Environ.* **2014**, *466–467*, 976–984.

[51] L. Li, C. Tang, Y. Zheng, B. Xia, X. Zhou, H. Xu, S.-Z. Qiao, *Adv. Energy Mater.* **2020**, *10*, 2000789.

[52] Z. Zhang, H. Zhao, Z. Wang, Z. Hu, Q. Wang, E. Meng, S. Lai, J. Ying, H. Li, C. Wu, *Environ. Res.* **2023**, *236*, 116794.

[53] D. Liu, X. Zhao, R. Su, Z. Hao, B. Jia, S. Li, L. Dong, *Processes* **2019**, *7*, 300.

[54] A. C. Ferrari, *Diamond Relat. Mater.* **2002**, *11*, 1053–1061.

[55] O. Beyssac, B. Goffé, J.-P. Petitet, E. Froigneux, M. Moreau, J.-N. Rouzaud, *Spectrochim. Acta Part A: Molecul. Biomolecul. Spectrosc.* **2003**, *59*, 2267–2276.

[56] G. Daniel, T. Kosmala, F. Brombin, M. Mazzucato, A. Facchin, M. C. Dalconi, D. Badocco, P. Pastore, G. Granozzi, C. Durante, *Catalysts* **2021**, *11*, 390.

[57] X. Zhang, P. Ma, C. Wang, L. Gan, X. Chen, P. Zhang, Y. Wang, H. Li, L. Wang, X. Zhou, K. Zheng, *Energy Environ. Sci.* **2022**, *15*, 830–842.

[58] A. M. Puziy, O. I. Poddubnaya, B. Gawdzik, M. Sobiesiak, *Adsorption* **2016**, *22*, 459–464.

[59] G. Y. Gor, M. Thommes, K. A. Cychosz, A. V. Neimark, *Carbon* **2012**, *50*, 1583–1590.

[60] J. Landers, G. Y. Gor, A. V. Neimark, *Colloid. Surf. A: Physicochem. Eng. Aspects* **2013**, *437*, 3–32.

[61] R. Padilla, H. Y. Sohn, *Metall. Trans. B* **1979**, *10*, 109–115.

[62] J. Rouquerol, P. Llewellyn, F. Rouquerol, in *Studies in Surface Science and Catalysis* (Eds.: P. L. Llewellyn, F. Rodriquez-Reinoso, J. Rouqerol, N. Seaton), Elsevier B.V., Amsterdam, 2007, pp. 49–56.

[63] W. Qiu, Y. Liu, M. Xie, Z. Jin, P. Li, G. Yu, *EES Catal.* **2024**, *2*, 202–219.